Image-based mesh generation for constructing a virtual representation of engineered wood product samples

European Journal of Wood and Wood Products

Patrick Grant[1*], Steven Psaltis[2], Maryam Shirmohammadi[3], Ian Turner[1]

[1*]School of Mathematical Sciences, Queensland University of Technology, Brisbane, Qld, Australia.
[2]School of Mechanical, Medical and Process Engineering, Queensland University of Technology, Brisbane, Qld, Australia.
[3]Forest Product Innovation, Queensland Department of Agriculture and Fisheries, Salisbury, Qld, Australia.

*Corresponding author(s). E-mail(s): p21.grant@qut.edu.au;

Electronic Supplementary Material 1 - Anatomical Images

Below are the two additional anatomical images (Figures 1 and 2) used to generate the thin and thick fractional radial position curves which are plotted in figure 3.

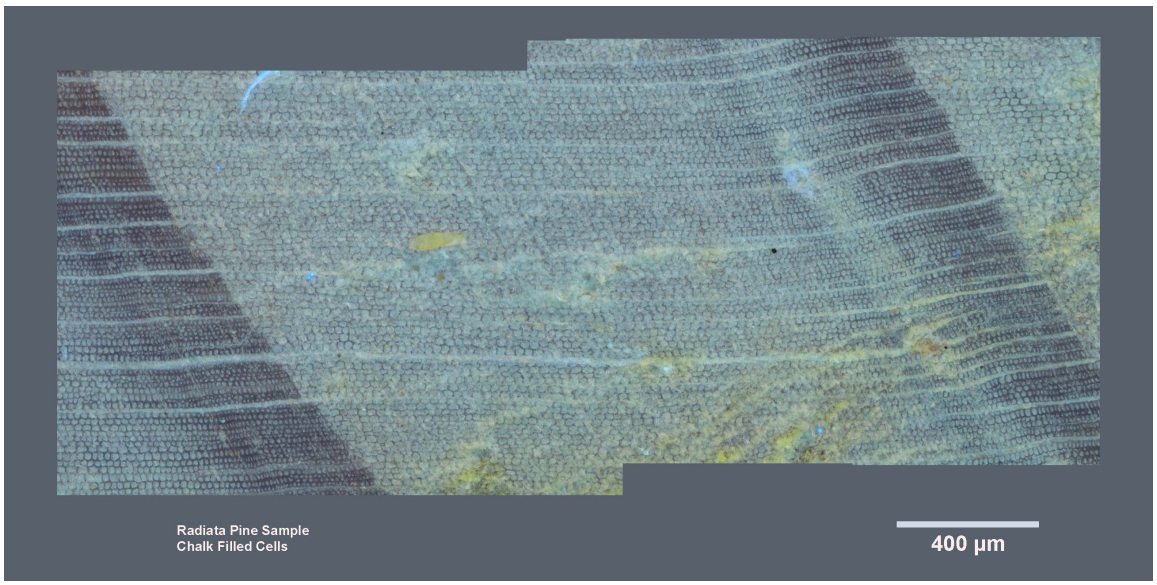

Fig. 1 Anatomical image of a radiata pine cross-section depicting a single growth ring, with a thin latewood band.

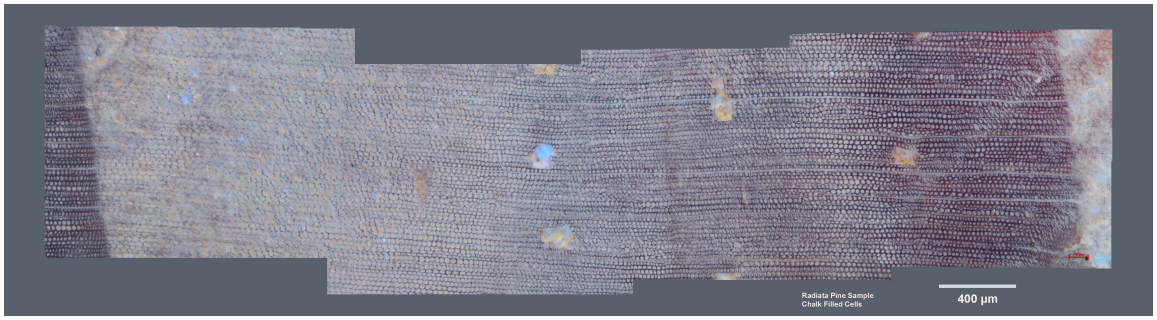

Fig. 2 Anatomical image of a radiata pine cross-section depicting a single growth ring, with a thick latewood band.

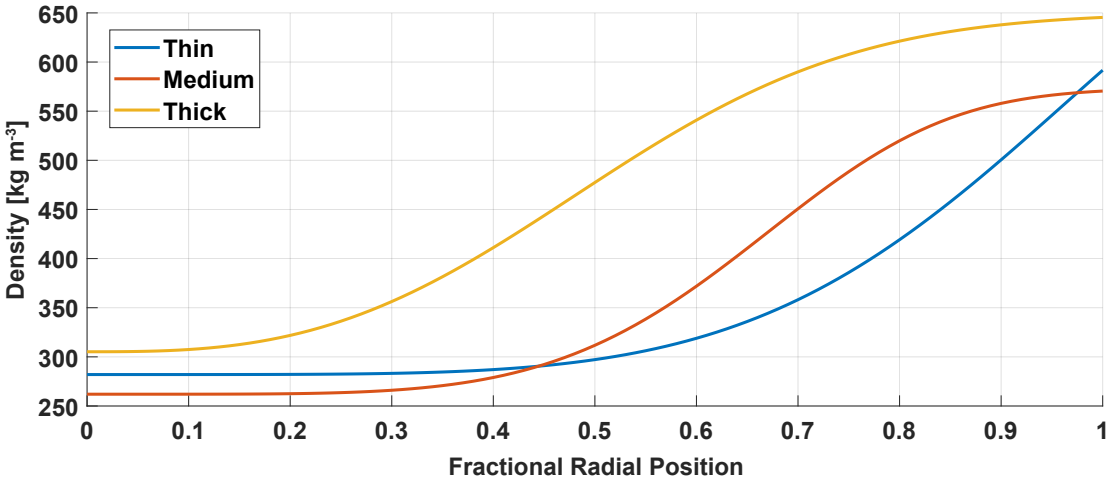

Fig. 3 Fitted five-point logistic curves for the three anatomical images.

Image-based mesh generation for constructing a virtual representation of engineered wood product samples

European Journal of Wood and Wood Products

Patrick Grant[1*], Steven Psaltis[2], Maryam Shirmohammadi[3], Ian Turner[1]

[1*]School of Mathematical Sciences, Queensland University of Technology, Brisbane, Qld, Australia.
[2]School of Mechanical, Medical and Process Engineering, Queensland University of Technology, Brisbane, Qld, Australia.
[3]Forest Product Innovation, Queensland Department of Agriculture and Fisheries, Salisbury, Qld, Australia.

*Corresponding author(s). E-mail(s): p21.grant@qut.edu.au;

Electronic Supplementary Material 2 - Iterations of Pith Location Algorithm

Below is six iterations of the pith location algorithm on a plainsawn timber sample.

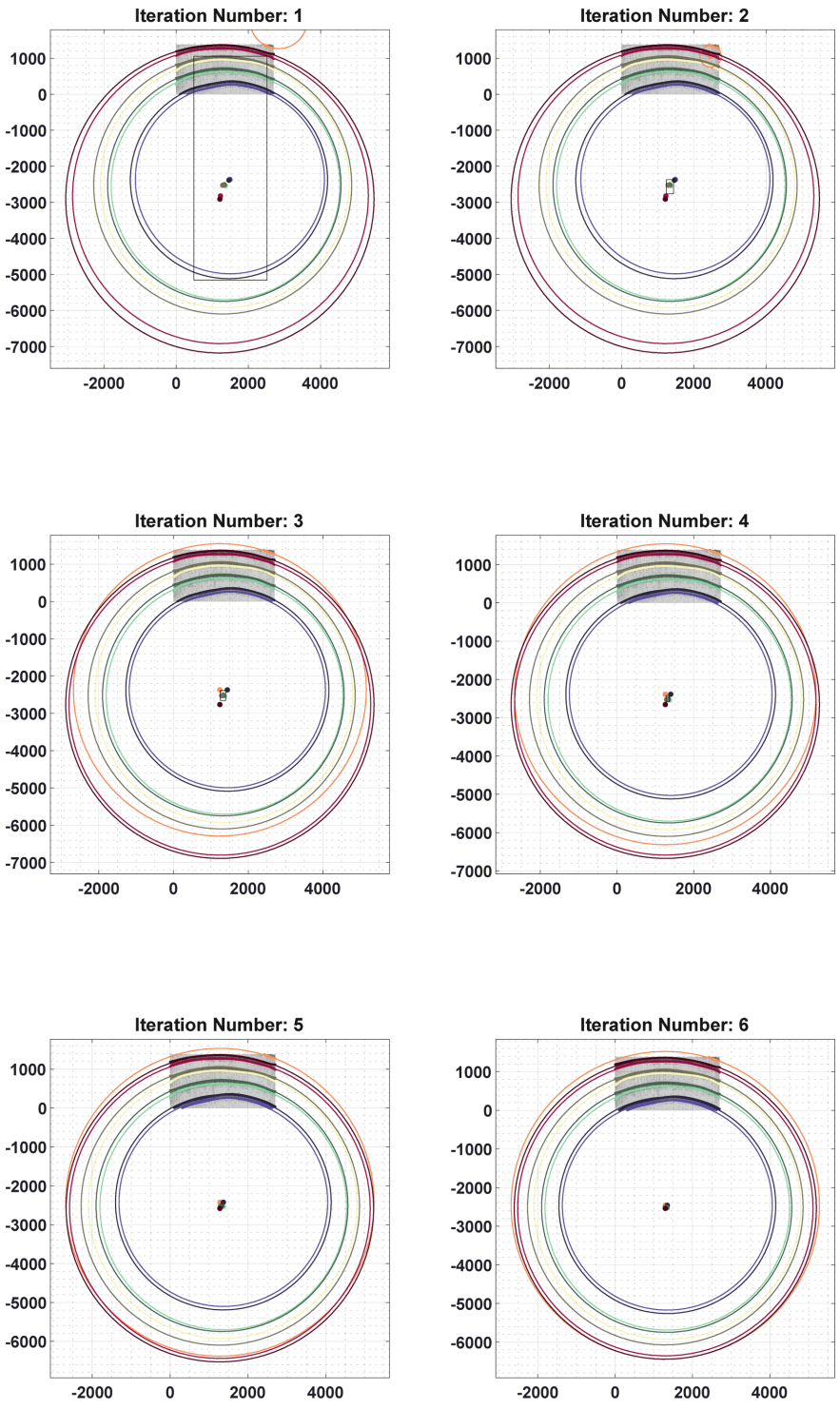

Fig. 1 Six iterations of pith location algorithm.[2]

Image-based mesh generation for constructing a virtual representation of engineered wood product samples

European Journal of Wood and Wood Products

Patrick Grant[1*], Steven Psaltis[2], Maryam Shirmohammadi[3], Ian Turner[1]

[1*]School of Mathematical Sciences, Queensland University of Technology, Brisbane, Qld, Australia.
[2]School of Mechanical, Medical and Process Engineering, Queensland University of Technology, Brisbane, Qld, Australia.
[3]Forest Product Innovation, Queensland Department of Agriculture and Fisheries, Salisbury, Qld, Australia.

*Corresponding author(s). E-mail(s): p21.grant@qut.edu.au;

Electronic Supplementary Material 3 - Validation of the Pith Location Algorithm

To evaluate the accuracy of the pith location algorithm, we conducted a validation study on three virtual cuts made within the log. The methodology, as described in section 2.6 of the manuscript, was applied to these three sections, which are presented in Figure 1. The algorithm determined the pith location at approximately 16 mm, 12 mm, and 6 mm away from the true pith for the blue, purple, and red virtual cuts, respectively. While the image quality was not sufficient to obtain a suitable image mask, the latewood rings in each sample were manually blacked out to provide a luminance of 0 in that pixel. It is worth noting that this masking procedure did not affect the validation of the pith location algorithm, which was the main focus of this investigation.

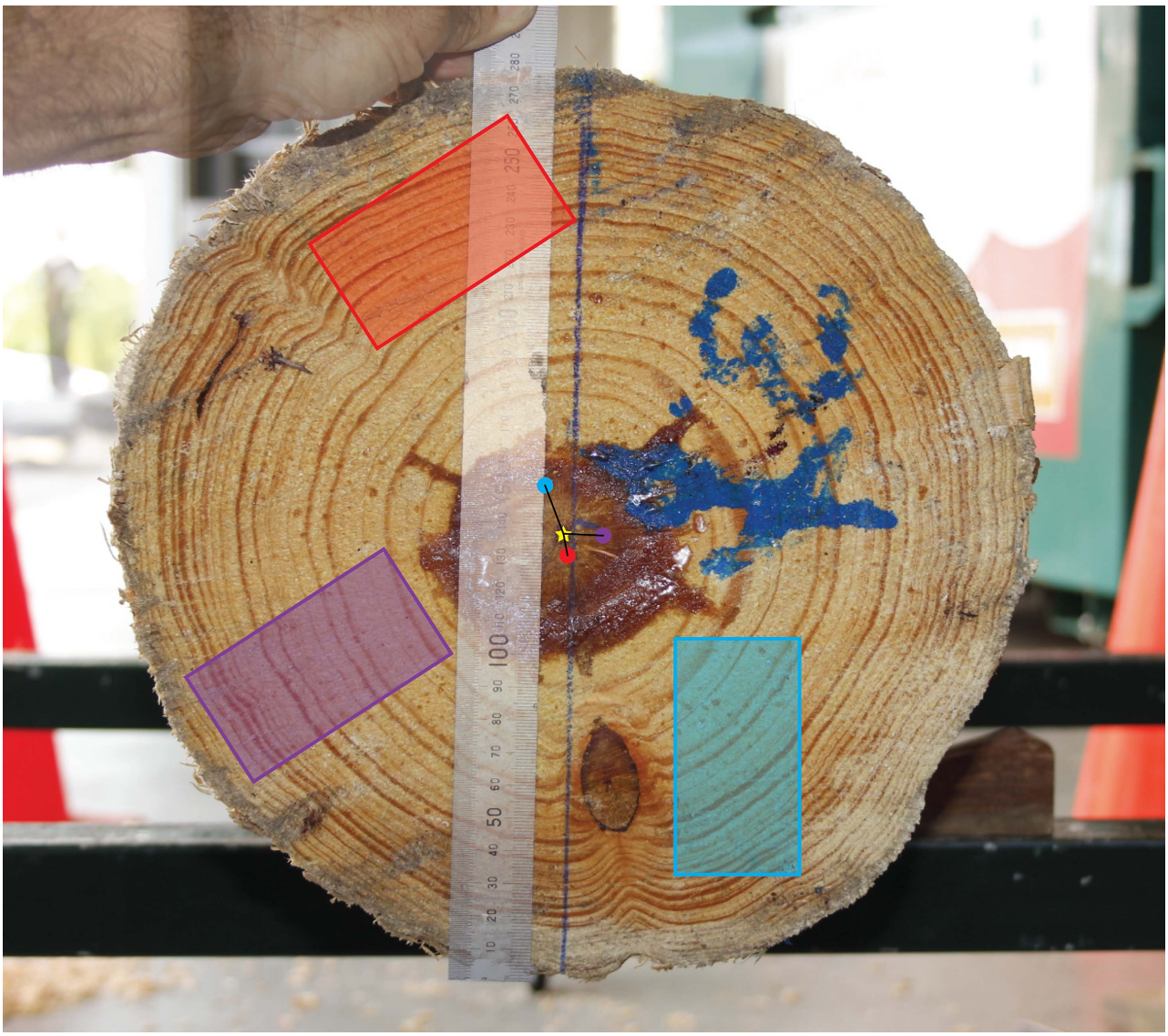

Fig. 1 The pith location algorithm tested on three sections of a swan log of radiata pine of approximately 28cm diameter. The coloured regions indicate the three different virtual cuts and the associated circle shows where the algorithm places the points where the yellow star is the true pith location. Image courtesy of Queensland Department of Agriculture and Fisheries (QDAF).

Image-based mesh generation for constructing a virtual representation of engineered wood product samples

European Journal of Wood and Wood Products

Patrick Grant[1*], Steven Psaltis[2], Maryam Shirmohammadi[3], Ian Turner[1]

[1*]School of Mathematical Sciences, Queensland University of Technology, Brisbane, Qld, Australia.
[2]School of Mechanical, Medical and Process Engineering, Queensland University of Technology, Brisbane, Qld, Australia.
[3]Forest Product Innovation, Queensland Department of Agriculture and Fisheries, Salisbury, Qld, Australia.

*Corresponding author(s). E-mail(s): p21.grant@qut.edu.au;

Electronic Supplementary Material 4 - Heat and Mass Transfer Model

The heat and mass transfer model that is numerically solved over the virtual representation to produce Figure 20 in the manuscript is the two-equation variant of the TransPore model that assumes the pressure of the board remains constant at the atmospheric value throughout the simulations. A brief description will be provided here; the reader is directed to (Perré and Turner, 1999) for the full heat and mass transfer model. The initial TransPore model was derived in the context of timber drying and consisted of three coupled nonlinear partial differential equations (PDEs) that govern the conservation of total water, energy and air. This model can be simplified to a two-equation model by assuming the gaseous pressure to remain constant at atmospheric

pressure. The transport equations that represent the water and energy phases are expressed as:

$$\frac{\partial \psi_\ell}{\partial t} + \nabla \cdot q_\ell = 0, \quad \ell = w, e,$$

where the conserved quantities and flux vectors are given as:

$$\psi_{\mathrm{w}} = \rho_0 X + \varepsilon_{\mathrm{g}} \rho_{\mathrm{v}}, \tag{1}$$

$$\psi_{\mathrm{e}} = \rho_0 (X h_{\mathrm{w}} + h_s) + \varepsilon_{\mathrm{g}} (\rho_{\mathrm{v}} h_{\mathrm{v}} + \rho_{\mathrm{a}} h_{\mathrm{a}}) - \int_0^{\rho_0 X_{\mathrm{b}}} \Delta h_{\mathrm{w}} \, \mathrm{d}\rho, \tag{2}$$

$$\mathbf{q}_{\mathrm{w}} = \rho_{\mathrm{w}} \mathbf{v}_{\mathrm{w}} + \rho_{\mathrm{b}} \mathbf{v}_{\mathrm{b}} - D_{\mathrm{eff}} \frac{\rho_{\mathrm{g}}}{1 - \omega_{\mathrm{v}}} \boldsymbol{\nabla} \omega_{\mathrm{v}}, \tag{3}$$

$$\mathbf{q}_{\mathrm{e}} = h_{\mathrm{w}} \rho_{\mathrm{w}} \mathbf{v}_{\mathrm{w}} + h_{\mathrm{b}} \rho_{\mathrm{b}} \mathbf{v}_{\mathrm{b}} - D_{\mathrm{eff}} \frac{\rho_{\mathrm{g}} h_{\mathrm{v}}}{1 - \omega_{\mathrm{v}}} \boldsymbol{\nabla} \omega_{\mathrm{v}} - K_{\mathrm{eff}} \boldsymbol{\nabla} T. \tag{4}$$

Table 1 provides a brief physical interpretation for each term in the model. The terms that are coloured red directly depend on the moisture content, temperature and crucially the local density throughout the domain. Again, further signifying the importance of using a mesh that accurately captures the growth ring structure. Note the correction factor of $1 - \omega_v$ introduced from the Stefan tube analogy in the vapour diffusion terms in the water and energy flux terms (Whitaker and Chou, 1983). The Stefan tube analogy is not suitable for high temperature and high pressure drying conditions, here the EWP sample is exposed only to atmospheric conditions (ambient temperature and related relative humidity), and this justifies our assumption.

The transport equations are discretised over the triangular prismatic mesh developed in this work, using the vertex centered finite volume method (see (Truscott and Turner, 2005) for an example). The resulting system of ordinary differential equations are then solving using the exponential Euler method (Carr et al, 2013). A reduced scale, two-layered CLT panel with visual description depicted in Figure 1(a) is considered in the moisture ingress application. The initial moisture content computed using the algorithm outlined in section 2.8 of the manuscript where the average moisture content is set to $\overline{X} = 0.5$ kg(water)/kg(dry solids) for both layers. The initial temperature is set to a temperature of $T = 25^\circ$ C everywhere. There are two

Table 1: Physical interpretation of the two-equation TransPore model.

Phase	Type	Term	Physical Interpretation
Water	Accumulation	$\rho_0 X$	Accumulation of free and bound water.
		$\varepsilon_\mathrm{g}\rho_\mathrm{v}$	Accumulation of water vapour in the gas.
	Flux	$\rho_\mathrm{w}\mathbf{v}_\mathrm{w}$	Advection of liquid water (Darcy's Law).
		$\rho_\mathrm{b}\mathbf{v}_\mathrm{b}$	Bound liquid flux.
		$D_\mathrm{eff}\frac{\rho_\mathrm{g}}{1-\omega_\mathrm{v}}\boldsymbol{\nabla}\omega_\mathrm{v}$	Diffusion of water vapour.
Energy	Accumulation	$\rho_0 X h_\mathrm{w}$	Enthalpy within the free water.
		$\rho_0 h_s$	Enthalpy within the solid phase.
		$\varepsilon_\mathrm{g}\rho_\mathrm{v}h_\mathrm{v}$	Enthalpy within the water vapour.
		$\varepsilon_\mathrm{g}\rho_\mathrm{a}h_\mathrm{a}$	Enthalpy within the air.
		$\int_0^{\rho_0 X_\mathrm{b}} \Delta h_\mathrm{w}\ \mathrm{d}\rho$	Integral heat of wetting.
	Flux	$\rho_\mathrm{w}h_\mathrm{w}\mathbf{v}_\mathrm{w}$	Advection of the liquid water enthalpy.
		$h_\mathrm{b}\rho_\mathrm{b}\mathbf{v}_\mathrm{b}$	Advection of the bound water enthalpy.
		$\rho_\mathrm{g}D_\mathrm{eff}\frac{h_\mathrm{v}}{1-\omega_\mathrm{v}}\boldsymbol{\nabla}\omega_\mathrm{v}$	Diffusion of the water vapour enthalpy.
		$K_\mathrm{eff}h_\mathrm{a}\boldsymbol{\nabla}T$	Heat conduction.

external boundary conditions used for this simulation which are referred to as saturating and atmospheric. The saturating condition is treated as a Dirichlet boundary condition where the moisture content at each boundary node is set to the maximum saturation calculated based on the nodal density value, refer to the face highlighted pink in Figure 1(b). The temperature also experiences a Dirichlet boundary condition fixing the temperature at the wet bulb condition is also imposed at these boundary nodes. All other faces are exposed to atmospheric conditions which depend on the dry bulb temperature and relative humidity. We model the variation of these conditions using simple trigonometric functions. The precise functional form of these boundary condition can be found elsewhere (see for example (Carr et al, 2011)). At the glue line interface between the two wood components, we employ imperfect boundary conditions for the moisture flux and perfect contact boundary conditions for the heat transfer by conduction. The exchange coefficients have been chosen to illustrate the transfer phenomenon evident there, and in future work will be calibrated using experimental data. The moisture and energy exchange between the two layers is governed by the parameter H_glue. When $H_\mathrm{glue} = 0$ there is no flux across the boundary, when it is large $H_\mathrm{glue} > 10$ the boundary is treated as perfect contact (Dirichlet condition), for intermediary values there is some proportion of flux that can travel over the glue line. We have assumed perfect contact for heat transfer across the glue line and arbitrarily chosen $H_\mathrm{glue} = 0.01$ for the moisture flux.

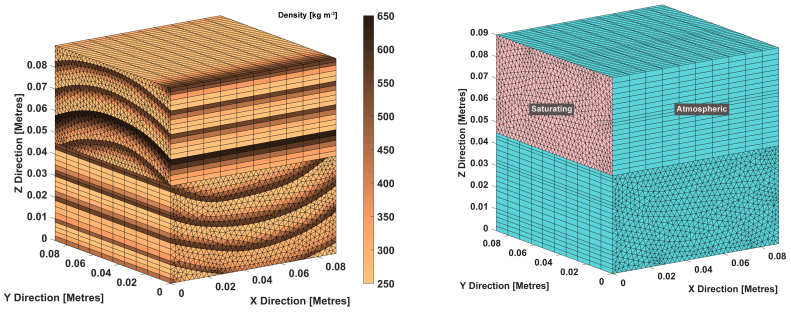

Fig. 1: (a) Elementwise density of the CLT panel sample. (b) Boundary conditions description for each face, the hidden faces are also experiencing atmospheric conditions.

References

Carr EJ, Turner IW, Perre P (2011) A new control-volume finite-element scheme for heterogeneous porous media: Application to the drying of softwood. Chemical engineering & technology 34(7):1143–1150. https://doi.org/10.1002/ceat.201100060

Carr EJ, Turner IW, Perre P (2013) A variable-stepsize jacobian-free exponential integrator for simulating transport in heterogeneous porous media: Application to wood drying. Journal of Computational Physics 233:66–82

Perré P, Turner IW (1999) A 3-d version of transpore: a comprehensive heat and mass transfer computational model for simulating the drying of porous media. International Journal of heat and mass transfer 42(24):4501–4521

Truscott S, Turner I (2005) A heterogeneous three-dimensional computational model for wood drying. Applied Mathematical Modelling 29(4):381–410

Whitaker S, Chou WT (1983) Drying granular porous media-theory and experiment. Drying technology 1(1):3–33